DE GRUYTER Nanophotonics 2020; 9(8): 2557–2567

Research article

Huanian Zhang[a,*], Pengfei Ma[a], Mingxiao Zhu, Wenfei Zhang, Guomei Wang and Shenggui Fu*

Palladium selenide as a broadband saturable absorber for ultra-fast photonics

https://doi.org/10.1515/nanoph-2020-0116
Received February 14, 2020; revised February 23, 2020; accepted February 23, 2020

Abstract: Air-stable broadband saturable absorbers (SAs) exhibit a promising application potential, and their preparations are also full of challenges. Palladium selenide ($PdSe_2$), as a novel two-dimensional (2D) layered material, exhibits competitive optical properties including wide tunable bandgap, unique pentagonal atomic structure, excellent air stability, and so on, which are significant in designing air-stable broadband SAs. In our work, theoretical calculation of the electronic band structures and bandgap characteristics of $PdSe_2$ are studied first. Additionally, $PdSe_2$ nanosheets are synthesized and used for designing broadband SAs. Based on the $PdSe_2$ SA, ultra-fast mode-locked operations in 1- and 1.5-μm spectral regions are generated successfully. For the mode-locked Er-doped operations, the central wavelength, pulse width, and pulse repetition rate are 1561.77 nm, 323.7 fs, and 20.37 MHz, respectively. Meanwhile, in all normal dispersion regions, mode-locked Yb-doped fiber laser with 767.7-ps pulse width and 15.6-mW maximum average output power is also generated successfully. Our results fully reveal the capacity of $PdSe_2$ as a broadband SA and provide new opportunities for designing air-stable broadband ultra-fast photonic devices.

[a]**Huanian Zhang and Pengfei Ma:** These authors equally contributed to this work.
***Corresponding authors: Huanian Zhang,** School of Physics and Optoelectronic Engineering, Shandong University of Technology, Zibo 255049, China; and Shandong Normal University, Jinan 250358, China, e-mail: huanian_zhang@163.com. https://orcid.org/0000-0001-7369-3379; and **Shenggui Fu,** School of Physics and Optoelectronic Engineering, Shandong University of Technology, Zibo 255049, China, e-mail: fushenggui@sdut.edu.cn
Pengfei Ma: State Key Laboratory of Luminescent Materials and Devices and Institute of Optical Communication Materials, South China University of Technology, Guangzhou 510640, China
Mingxiao Zhu, Wenfei Zhang and Guomei Wang: School of Physics and Optoelectronic Engineering, Shandong University of Technology, Zibo 255049, China

Keywords: palladium selenide; broadband saturable absorber; air-stable ultra-fast devices; mode-locked lasers.

1 Introduction

The emergency of two-dimensional (2D) layered materials provided exciting opportunities for the development of novel opto-electric, bio-medical, and energy devices [1–13]. Recently, novel ultra-fast optical devices such as Q-switchers, mode-lockers, optical switchers, and so on have been investigated extensively due to their excellent opto-electric characteristics including wide-absorption band, ultra-fast recovery time, high-damage threshold, etc. [1–5]. Especially, 2D material-based mode lockers were widely employed for proposing ultra-fast pulsed fiber lasers, which have important applications in the fields of medicine, optical spectroscopy, chemical and biomedical researches, and so on [1–3, 14–20]. In addition, 2D material-based mode-locked fiber lasers were also regarded as excellent test platforms for the research of various kinds of soliton phenomena, promoting the rapid progress of 2D ultra-fast device-based soliton research [21].

Graphene was the pioneer in exploring ultra-fast applications of 2D materials and exhibited excellent performance in demonstrating pulsed fiber laser operating from visible to mid infrared bands [22–29]. As is known, the zero-bandgap structure of graphene also brought great obstacles to its optoelectronic device applications. Since then, inspired by graphene, various 2D layered materials including multi-elemental (transition metal dichalcogenides (TMDs) [30–41], topological insulator (TIs) [42–47], ferromagnetic insulator (FIs) [48–50], metal chalcogenide [51, 52], MXenes [53–56], etc.) and mono-elemental (Xenes (phosphorene [57–66], graphdiyne [67], antimonene [68], bismuthene [69–71], tellurene [72, 73]) and selenene [74]) were prepared as mode lockers for obtaining pulsed fiber lasers extensively. Among which, black phosphorus (BP) was regarded as an ideal saturable absorption material due to its obvious advantages of a tunable bandgap value of 0.3–1.5 eV [57–59], high nonlinear coefficient, and so on. However, the air-unstable property of

BP also limited its wide in-deep photoelectric applications. In general, exploring air-stable materials with wide tunable bandgap value is of great significance in promoting the practical optical device applications of 2D materials.

In our contribution, $PdSe_2$ was selected as the base material for designing wide absorption-band ultra-fast optical devices. Reported results have proven that $PdSe_2$ exhibited several competitive excellent properties. Most importantly, $PdSe_2$ exhibits a thickness-dependent wide-tunable bandgap value, which can be narrowed from 1.3 eV for the monolayer to 0 eV for bulk [75–81]. Moreover, as is known that the thickness-dependent bandgap is not a unique property of $PdSe_2$ [82, 83], the thickness-dependent bandgap is regarded as a commonality of two-dimensional materials. However, in comparison with $PdSe_2$, the bandgaps of commonly reported TMDs (MoS_2, WS_2, SnS_2, etc.) always vary between 1 and 2 eV. In other words, 2D materials with such a widely tunable band gap as $PdSe_2$ were rarely reported before. Such a competitive wide optical bandwidth coverage is the most unique advantages of $PdSe_2$ compared with other types of 2D materials, indicating that $PdSe_2$ is a promising material for preparing wide absorption band photoelectric devices. Second, in comparison to other isotropic TMDCs, $PdSe_2$ has another unique property of pentagonal atomic structure in which Pd atoms coordinate with four Se atoms, forming a square backbone lattice (Figure 1A and B). The waved Pd–Se layers are held together by van der Waals force with a distance of about 0.4 nm (Figure 1C) [77–81]. Owing to the unique pentagonal atomic structure, in comparison with commonly used TMDs, $PdSe_2$ devices present a unique anisotropic response to external stimulations, which will provide opportunities for designing anisotropic photoelectric devices. Especially, $PdSe_2$ also has the essential basic properties used as the optoelectronic device: excellent air stability [80]. Besides, high-quality $PdSe_2$ nanosheets can be easily prepared by the cost-effective liquid-phase exfoliation (LPE) method. All the mentioned properties indicate that $PdSe_2$ is an excellent air-stable low-cost nonlinear absorption material with wide absorption bandgap. Previously, the nonlinear absorption applications of $PdSe_2$ have been investigated within solid state lasers preliminarily [84, 85]. Besides that, the thickness-dependent wide-band ultra-fast optical applications of $PdSe_2$ are still far from thoroughly investigated. Exploring the wide-band absorption applications of $PdSe_2$ and designing $PdSe_2$-based broadband optical devices are meaningful for promoting the practical development of 2D-based ultra-fast optical devices.

In this work, first, based on the density function theory, the electronic band structures and bandgap characteristics are calculated. The calculated results prove that $PdSe_2$ exhibits a wide tunable indirect bandgap of 0–1.3 eV, which is suitable for designing broadband ultra-fast optical devices. In addition, $PdSe_2$ nanosheets with 15- to 16-layer thickness are prepared and employed for proposing as an saturable absorber (SA) successfully. Based on the $PdSe_2$ SA, within all anomalous dispersion regions, a mode-locked Er-doped fiber laser with a 323.7-fs pulse width under a pulse repetition rate of 22.7 MHz is obtained. Meanwhile, within all normal dispersion regions, a mode-locked Yb-doped fiber laser with a 767.7-ps pulse width and 15.6-mW maximum average output power is also generated successfully. The excellent wide-band absorption performance of $PdSe_2$ presents that $PdSe_2$ exhibits great potential and capacity in designing wide absorption band ultra-fast optical devices.

2 Density function theory (DFT) calculation

In our work, the Vienna ab initio simulation package (VASP, University of Vienna) was employed to optimize crystal structures and calculate electronic structures with

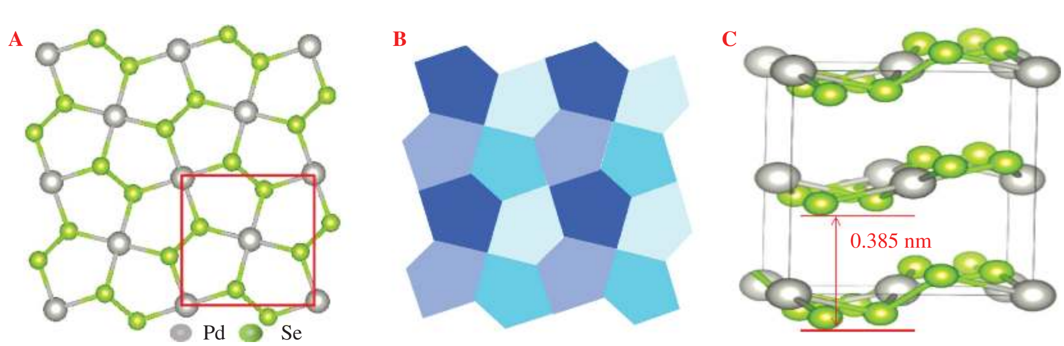

Figure 1: Atomic structures of $PdSe_2$.
(A) Top view of a 2×2×1 supercell of the single-layer $PdSe_2$. (B) A sketch of the Cairo tessellation formed from pentagons. (C) Side view of the three-layer $PdSe_2$.

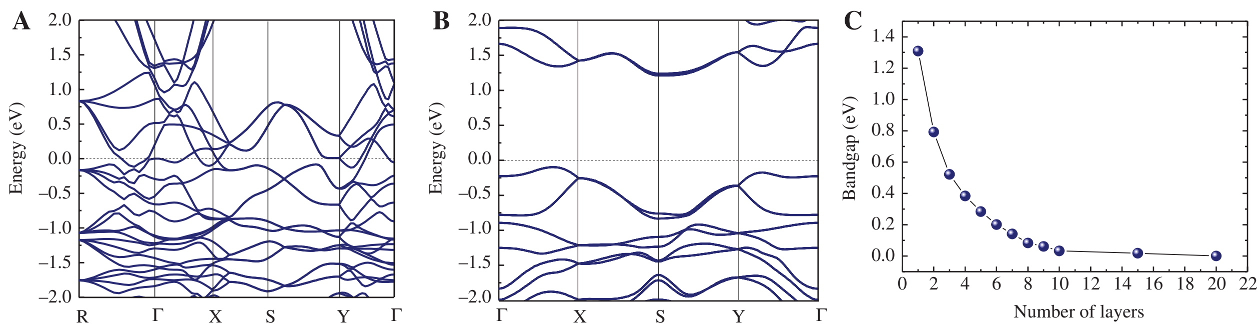

Figure 2: Calculated results of the electronic band structures and bandgap values.
Electronic band structures of (A) bulk $PdSe_2$ and (B) single-layered $PdSe_2$. (C) Relationship between the bandgap value and layer number.

the framework of density functional theory [86, 87]. We tested several functionals implemented in VASP, including PBE [88], optPBE [89], optB88 [89], PBE-D2 [90], PBE-D3 [91], and PBE-TS [92]. It is found that the functional of optPBE yields reasonable results for structural and electronic and properties. The energy cutoff for the plane-wave basis was set to 500 eV for all calculations and the k-point spacing of the reciprocal space was fixed to 0.02 $Å^{-1}$. All atoms were relaxed until the residual forces were below 0.001 eV/Å. For the 2D slab calculations (monolayer and few-layer $PdSe_2$ systems), a vacuum region of at least 20 Å in the out-of-plane direction was used to avoid spurious interactions with periodic images.

The calculated electronic band structures of bulk and single-layer $PdSe_2$ are provided in Figure 2A and B, respectively. For the bulk $PdSe_2$, no bandgap is recorded. Meanwhile, the single-layered $PdSe_2$ exhibits an obvious indirect bandgap of about 1.31 eV, which is close to its direct bandgap of 1.43 eV. The relationship between the bandgap value and layer number is also calculated and shown in Figure 2C. As is shown, when the layer number increases from 1 to 15, the bandgap value decreases from 1.31 to 0.02 eV. In addition, the bandgap values for 20 layers and bulk $PdSe_2$ are 0 and −0.01 eV, respectively, which also proves that bulk $PdSe_2$exhibits no bandgap. Especially, such a large tunable bandgap is of great significance for designing broadband opto-electronic devices.

3 Preparation and characteristics of the $PdSe_2$

Because $PdSe_2$ exhibits excellent air stability, thus, in our work, $PdSe_2$ nanosheets were prepared by the commonly used low-cost LPE method. The preparation process is provided in Figure 3 (progress 1) and described as follows: 10 mg $PdSe_2$ powder is added into 100 ml of ethanol for soaking for about 96 h. The soaked soliton is kept under ice-bath sonication for 24 h. The sonication is beneficial for stripping a few layers of the $PdSe_2$ nanosheets. After that, the suspension is centrifuged for 30 min at 5000 rpm to obtain few-layered $PdSe_2$ nanosheet dispersion. Finally, the dispersed $PdSe_2$ nanosheets is mixed with 100 ml of 5 wt% polyvinyl alcohol (PVA) solution and placed in the ultrasonic cleaner for another 6 h to obtain a uniform $PdSe_2$-PVA solution. In preparing the 2D material-based $PdSe_2$-PVA SA with good stability characteristics, a novel preparation method for isolating the oxygen and the materials, reported in our previous work [37], is employed. The preparation process is also provided in Figure 3 (progress 2) and described as follows: first, a thin liquid glass film is spin coated on the sapphire substrate. After solidification of the liquid glass, a thin $PdSe_2$-PVA film is spin coated on the surface of the liquid glass. Then, another liquid glass film is spin coated on the 2D materials to isolate the oxygen. In addition, another sapphire is coated on the liquid glass resulting in a five-layer sandwich structure. Finally, the sapphire substrates on both sides are removed, and the remaining structure is polished and cut to 1×1 mm^2 for proposing as SA, which is under the protection of the two outer glass films. In our experiment, the prepared three-layer glass-$PdSe_2$-glass material was inserted between two fiber ferrules so as to be easily integrated into the fiber laser cavity acting as a mode locker.

Figure 4 depicts the characterized results including Raman, transmission electron microscope (TEM), and atomic force microscope (AFM), which are beneficial in understanding the layered structure and saturable absorption characteristics of the $PdSe_2$ nanosheets. Figure 4A gives the Raman spectrum of the $PdSe_2$ powder recorded by a Raman spectrometer (Horiba HR Evolution). Four obvious Raman peaks located at 143.6, 205.3, 220.8, and 255.7 cm^{-1} are presented, which correspond to the A_g^1, A_g^2, B_{1g}, and A_g^3 Raman active modes of $PdSe_2$ [78–80]. In general, the Raman characteristics of the $PdSe_2$ nanosheets should be studied as a comparison. However,

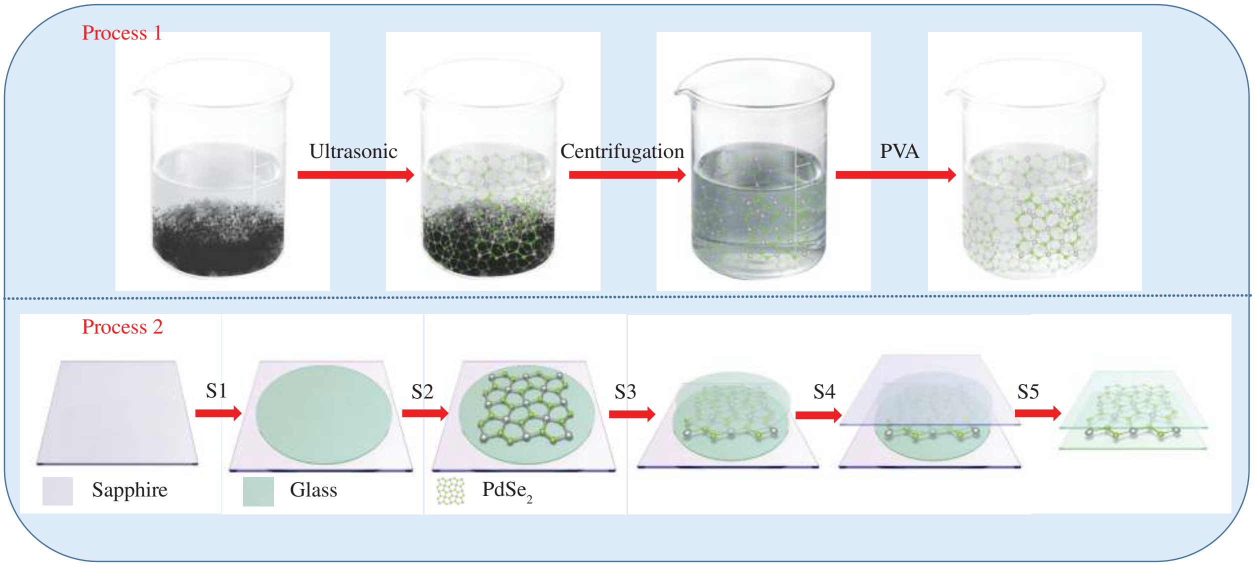

Figure 3: Preparation process of $PdSe_2$ nanosheets and $PdSe_2$-PVA SA.

in our experiment, after centrifugation, the concentration of $PdSe_2$ nanosheets in the solution is too dilute for testing their Raman characteristics. Therefore, for the further detailed characterization of the layered structure characteristics of the $PdSe_2$ nanosheets, their structure characteristics of $PdSe_2$ nanosheets are further characterized by TEM and AFM. The TEM and high-resolution TEM (HRTEM) images are shown in Figure 4B–D. As shown in Figure 4B, the $PdSe_2$ nanosheets exhibit an obvious layered structure. Clear crystal lattices with a d-spacing of ~0.4 nm are depicted in Figure 4C and D, indicating that the prepared $PdSe_2$ nanosheets possess excellent layered structure and crystallinity properties. After the preparation progress including soaking, ultrasonic, and centrifugation, the maintained layered structure and crystallinity indicates that the $PdSe_2$ material exhibits excellent air-stable properties, As is mentioned, $PdSe_2$ exhibits a wide tunable thickness-dependent bandgap and corresponding nonlinear optical properties. Thus, the thickness characteristics have great significance in designing $PdSe_2$-based broadband devices. Based on an atomic force microscope (AFM, Bruker Multimode 8, Bruker, Karlsruhe, Germany), the thickness characteristics are recorded and shown in Figure 4E and its inset. As is shown, the prepared $PdSe_2$ nanosheets exhibit uniform thickness and flat surface. In addition, overlapping phenomenon also occurs between the nanosheets (the inset in Figure 4E). The corresponding thicknesses of the marked areas of Figure 4E are provided in Figure 4F. The thicknesses of the $PdSe_2$ are about 6 nm, corresponding to ~15–16 layers [80], presenting a small fluctuation of thickness. The AFM results prove that $PdSe_2$ nanosheets with uniform thickness characteristics were prepared successfully.

For an SA, its nonlinear optical properties including saturation intensity, modulation depth, and nonsaturable loss are basic and important for evaluating its nonlinear absorption performance. In our experiment, based on a commonly used power-dependent transmission technique, the nonlinear optical properties of the $PdSe_2$ SA were investigated experimentally. The experimentally setup is shown in the inset of Figure 5A. As is shown, pulsed laser is employed as the pump source. In the experiment, homemade mode-locked Yb-doped and Er-doped fiber lasers are used as the pump source for testing the nonlinear optical properties of $PdSe_2$ SA within 1 and 1.5 µm regions, respectively. A variable optical attenuator (VOA) is used for adjusting the pump intensity continuously. The pump intensity is divided into two parts through a 50:50 output coupler (OC). One part is used for testing the SA and recorded by a power meter (PM2) and another part is recorded by PM1 directly as a comparison. Thus, the experimental transmission data can be calculated by the results recorded by PM1 and PM2. Calculated transmission results of the $PdSe_2$ SA are shown in Figure 5A and B. Additionally, the experiment results can be fitted according to a simple two-level model as follows [1–3]:

$$T(I) = 1 - \Delta T \cdot \exp\left(-\frac{I}{I_{sat}}\right) - T_{ns}$$

where $T(I)$, ΔT, I, I_{sat}, and T_{ns} are the transmission, modulation depth, input pulse energy, saturation intensity,

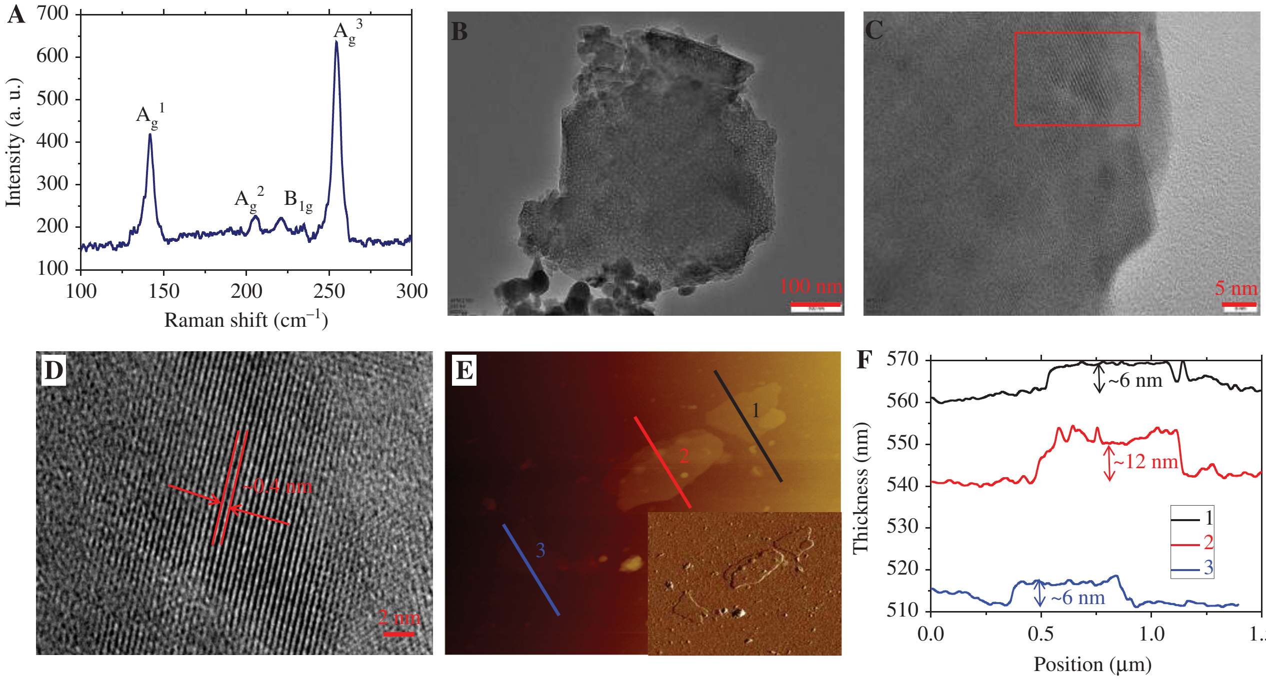

Figure 4: Characterized results of the $PdSe_2$.
(A) Raman spectrum of the $PdSe_2$ powder. (B) TEM image of the $PdSe_2$ nanosheets. (C, D) HRTEM images of the $PdSe_2$ nanosheets. (E) AFM image of the prepared $PdSe_2$ nanosheets. (E) Inset: The corresponding morphology of the $PdSe_2$ nanosheets recorded with the AFM. (F) The corresponding thickness characteristics.

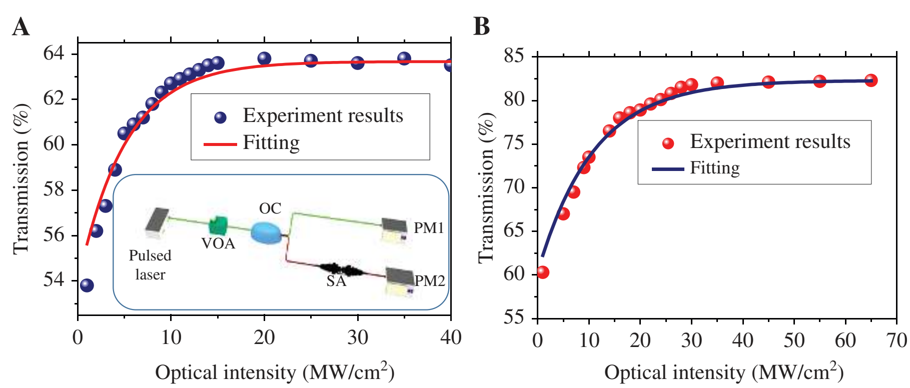

Figure 5: Nonlinear optical absorption properties of the $PdSe_2$-SA.
(A) Within 1-µm region. (B) Within 1.5-µm region. (A) Inset: The experimental setup used for testing nonlinear optical properties.

and non-saturable loss, respectively. Finally, the saturation intensity, modulation depth, and the saturable loss of the $PdSe_2$ SA at 1064 nm are 5.01 MW/cm², 9.7%, and 36.2%, respectively. Meanwhile, at 1550 nm, the corresponding data are 15.63 MW/cm², 22.1%, and 17.9%, respectively.

As a typical 2D material, the saturable absorption mechanism can be explained by the Pauli blocking principle [70, 73]. The progress of the absorption is shown in Figure 6. First, under low excitation intensity, linear absorption will occur. As is shown, when the energy of the incident light is larger than the bandgap value of the $PdSe_2$, electrons distributed in the valence band can absorb the energy of the incident light and be excited into the conduction band. After that, the hot electrons cooled almost immediately and led to the formation of a hot Fermi-Dirac distribution. Under this condition, the newly created electron-hole pairs will block the originally potential interband optical transitions around the Fermi energy (-E/2) and the absorption of photons. Finally,

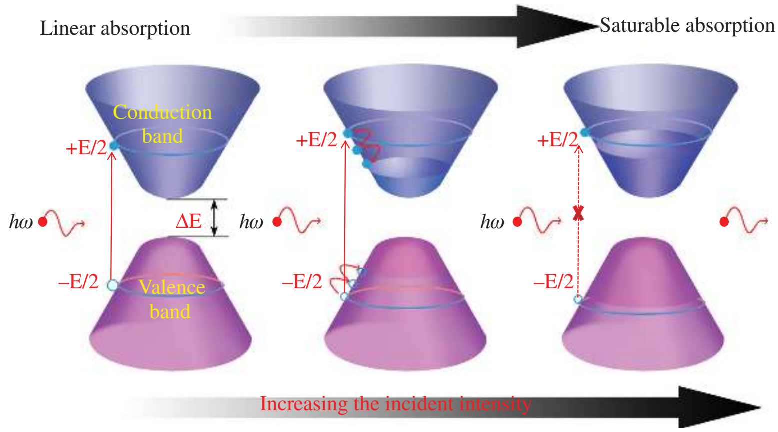

Figure 6: Saturable absorption mechanism of $PdSe_2$.

electrons and holes recombine and reach to an equilibrium distribution state due to the intraband phonon scattering. However, under a higher excitation intensity, the concentration of photocarriers increase instantaneously, and the energy states near the edge of the conduction and valence band will be filled. The absorption will be blocked due to the fact that no two electrons can reach the same state defined by the Pauli blocking principle. Thus, specific frequency photons transmit the material without absorption. As is described, the bandgap value is of great significance in designing ultra-fast photonics devices. Combined with the characterized results shown in Figure 4F and the simulation results provided in Figure 2C, the thickness of the $PdSe_2$ nanosheets used in our experiment is about 15–16 layers, corresponding to a narrow bandgap width of about 0.02 eV ($6.2 * 10^4$ nm). Thus, by adjusting the layer numbers, $PdSe_2$-based ultra-fast photonics devices with an expectant bandgap can be easily prepared. Besides, such a narrow bandgap value indicates that $PdSe_2$ is also an excellent candidate for developing wide-absorption band photonics devices covering almost the entire optical band.

4 Results and discussion

4.1 Mode-locked Er-doped operation

The absorption performance of the $PdSe_2$-PVA SA was tested within an Er-doped fiber laser for the first time. The experimental setup of the $PdSe_2$-PVA-based mode-locked Er-doped fiber laser is depicted in Figure 7A. A commonly used ring laser cavity consisting of a 980/1550 wavelength division multiplexer (WDM), a 0.23-m-long high doping concentration Er-doped fiber (EDF; Liekki, Er-110, 4/125), a polarization-independent isolator (PI-ISO), two polarization controllers (PCs), a 20/80 output coupler (OC), and the prepared $PdSe_2$-PVA SA is demonstrated. A 400-mW/976-nm laser diode, acting as the pump source, is injected into the laser cavity through the WDM. The PCs, OC PI-ISO, and $PdSe_2$-PVA are used for adjusting the polarization states, outputting the energy, ensuring the unidirectional transmission, and acting as a mode locker within the ring laser cavity, respectively. The total length of the laser cavity is 10.09 m including 0.23 m of EDF and 9.86 m of single-mode fiber (SMF). The dispersion value of the EDF and SMF are −9 and 18 ps/nm/km [17], respectively. Thus, the net dispersion value of the cavity is calculated to be about −0.22 ps^2. The output characteristics of the mode-locked laser operation are tested by an optical spectrum analyzer (OSA; AQ6317B, Yokogawa, Tokyo, Japan), a 3-GHz photo-detector, a digital oscilloscope (DPO4054, Tektronix, Beaverton, OR, USA), a spectrum analyzer (R&S FPC1000, Jena, Germany), an auto-correlator (FR-103XL, Femtochrome, Berkeley, CA, USA), and a power meter (PM100D-S122C, Thorlabs, Newton, NJ, USA).

In the experiment, when the pump power was higher than 89 mW, mode-locked operation can be recorded by adjusting the PCs carefully and maintained to be stable with the pump power increasing from 89 to 356 mW, the maximum average output power was 3.66 mW, corresponding to an optical-to-optical conversion efficiency of 1.03%. The emission optical spectrum is provided in Figure 7B. Obvious Kelly sidebands are depicted in the spectrum, indicating that the mode-locked operation corresponds to the traditional soliton (TS) region. The central wavelength (λ_c) and the spectral full width at half maximum (FWHM) are 1561.77 and 9.33 nm, respectively. The pulse train of the mode-locked operation is shown in Figure 7C. The

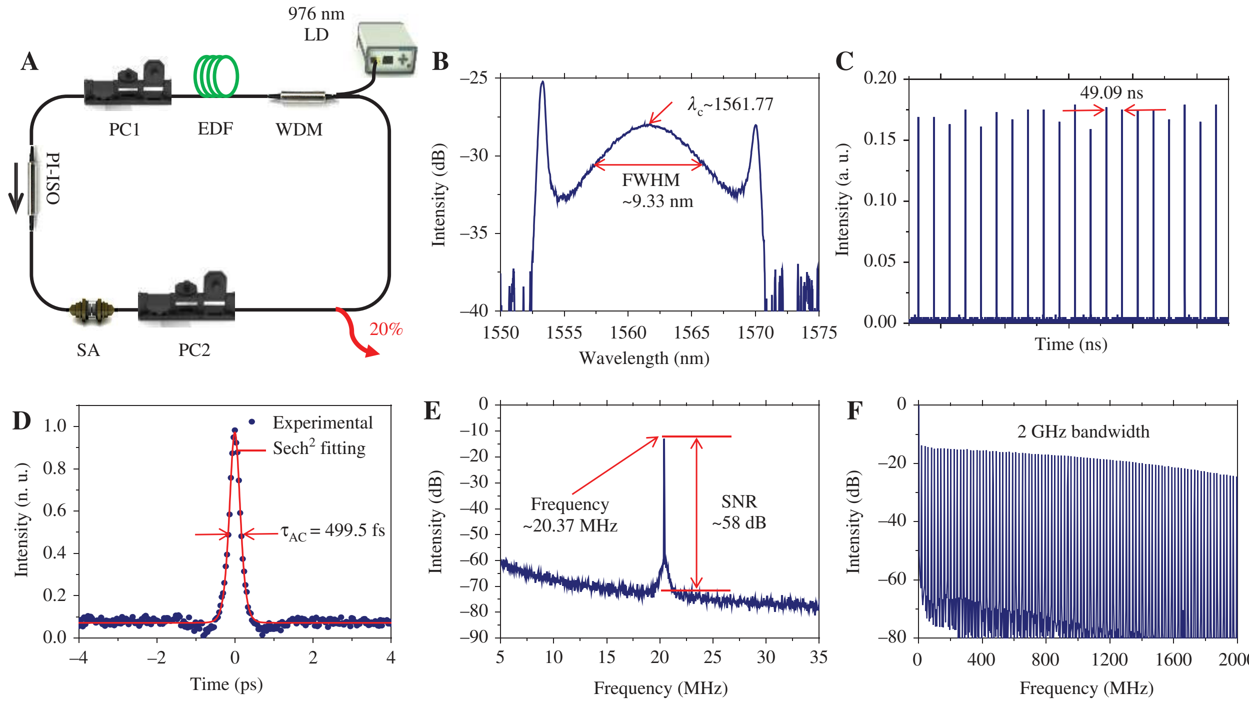

Figure 7: Experimental setup and output characteristics of the $PdSe_2$-based mode-locked Er-doped fiber laser.
(A) Experimental setup. (B) Emission optical spectrum. (C) The recorded pulse train. (D) The measured auto-correlation trace. (E) RF spectrum located at 20.37 MHz. (F) RF spectrum recorded under 2 GHz bandwidth.

pulse-to-pulse time is 49.09 ns, corresponding to a pulse repetition rate of 20.37 MHz, which is in agreement with the cavity-length value ($f = c/nl$, where f, c, n, and l are the pulse repetition rate, velocity of light, refractive index, and the length of the cavity, respectively). Besides, it is obvious that the pulse trains are not uniform. In addition, no period doubling or periodicity phenomenon reported in previous works [93, 94] was recorded in the experiment, indicating that the fluctuation of the pulses can be further eliminated. The measured auto-correlation trace is provided in Figure 7D. As is shown, the FWHM of the pulse is about 499.5 fs, assuming a $sech^2$ temporal profile calculation for TS operation. The real pulse duration is about 323.7 fs (499.5 * 0.648 fs). Thus, combined with the mentioned 9.33-nm spectrum width, the time-bandwidth product (TBP) is about 0.37, which is slightly larger than the theoretical transform limit value (0.315) and indicates that the soliton pulse is a little chirped. For the mode-locked operation, its stability characteristics are tested by the spectrum analyzer. Radio frequency (RF) spectrum recorded within 30-MHz width is provided in Figure 7E, the central frequency is located at 20.37 MHz, and the signal-to-noise ratio (SNR) is as high as 58 dB, indicating that the mode-locked operation exhibits excellent stability characteristics. The RF spectrum within 2-GHz width is also depicted in Figure 7F for further revelation of its high stability characteristics.

4.2 Mode-locked Yb-doped operation

For future testing of the broadband absorption performance of the $PdSe_2$ SA, a mode-locked Yb-doped fiber (YDF) laser was also demonstrated in our work. An almost identical experimental setup as provided in Figure 7A is employed and shown in Figure 8A. Under this condition, the laser gain medium is a 0.36-m YDF (Liekki, Yb-1200, 4/125). The total length is about 60.97 m including 0.36 m YDF and 60.61 m SMF (Hi-1060) used for adjusting the dispersion value of the laser cavity. The dispersion value of the YDF and SMF are −43 and −42 ps/nm km, respectively. Thus, the net dispersion value of the cavity is calculated to be about 1.54 ps^2. Mode-locked pulses are delivered out the cavity through a 10% port of a 10/90 OC.

Stable mode-locked pulses were recorded when the pump power is higher than 135 mW by adjusting the polarization state carefully. In the experiment, the mode-locked state was maintained to be stable with the pump power increasing from 135 to 338 mW. The maximum average output power was as high as 15.6 mW, corresponding to an optical-to-optical conversion efficiency of 4.6%. The output characteristics of the $PdSe_2$-based mode-locked YDF laser are provided in Figure 8. The emission spectrum locates at the central wavelength of 1067.37 nm

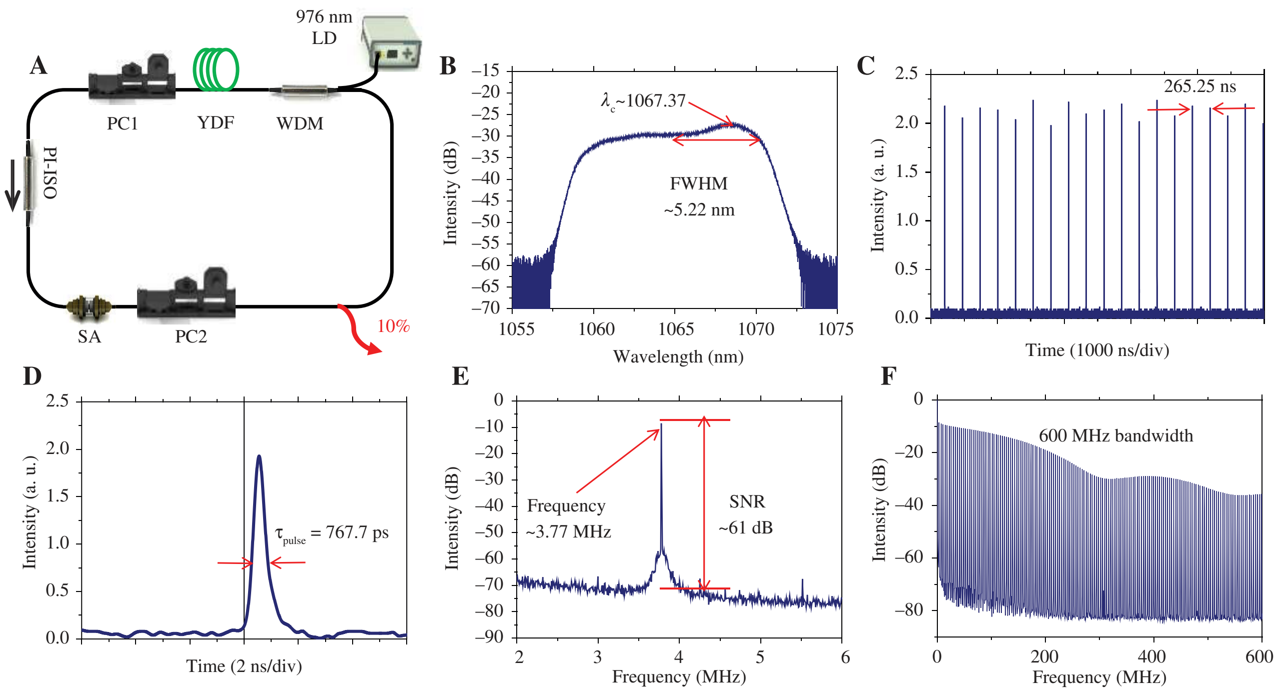

Figure 8: Experimental setup and output characteristics of the $PdSe_2$-based mode-locked Yb-doped fiber laser. (A) Experimental setup. (B) Emission optical spectrum. (C) The recorded pulse train. (D) The single pulse shape. (E) RF spectrum located at 3.77 MHz. (F). RF spectrum recorded under 600 MHz bandwidth.

with an FWHM of 5.22 nm (Figure 8B). Figure 8C gives the typical pulse train of the mode-locked laser. The pulse-to-pulse time is 265.25 ns, corresponding to a pulse repetition rate of 3.77 MHz, which also matches well with the cavity length. Fluctuation of the mode-locked pulses is also recorded as described in the mode-locked Er-doped laser. The single-pulse shape is provided in Figure 8D, the pulse width is about 767.7 ps. However, due to lack of a higher speed oscilloscope with shorter rise time, the real width of the pulse is not recorded. In addition, the pulse width characteristics were also checked by the auto-correlator; however, no pulse peaks were tested, indicating that the pulse width is wider than 90 ps. As mentioned, the spectrum width was 5.22 nm, corresponding to a theoretical pulse width of ~0.33 ps. All the results prove that the mode-locked pulses are highly chirped due to the large dispersion value. The RF spectra are also recorded for examining the stability characteristics of the mode-locked operations. The results are described in Figure 8E and F. As is shown in Figure 8E, the central frequency locates at 3.77 MHz, and the SNR is as high as 61 dB. The wideband RF spectrum (Figure 8F) also proves that the mode-locked operations exhibit excellent stability properties. Additionally, it needs to be emphasized that, in our experiment, it takes about 1 month from the preparation and nonlinear characterization of the $PdSe_2$ SA to its ultrafast laser applications. During the long-period investigation, $PdSe_2$ SA is preserved at normal temperature. As described above, it still exhibited good saturable absorption performance, proving that the $PdSe_2$ SA has excellent air stability.

In conclusion, the electronic band structures and bandgap characteristics of $PdSe_2$ are calculated theoretically. The bandgap value of $PdSe_2$ is calculated to be 0–1.3 eV, indicating that $PdSe_2$ was a promising material for designing broadband optical devices. In the experiment, $PdSe_2$ nanosheets were prepared with the LPE method and used for designing a new structure SA. Its broadband nonlinear absorption performance was characterized within Er- and Yb-doped fiber laser, respectively. The experiment results present $PdSe_2$ as exhibiting good performance in demonstrating ultra-fast pulsed lasers and great significance in designing broadband ultra-fast optical devices, which provide meaningful reference for designing air-stable broadband ultra-fast photonic devices.

Acknowledgment: This work was supported by the National Science Foundation of China (Grant No. 11904213, Funder Id: http://dx.doi.org/10.13039/501100001809).

Conflict of interest: The authors declare no conflicts of interest.

References

[1] Guo B, Xiao QL, Wang SH, et al. 2D layered materials: synthesis, nonlinear optical properties, and device applications. Laser Photonics Rev 2019;13:1800327.
[2] Guo SY, Zhang YP, Ge YQ, et al. 2D V-V binary materials: status and challenges. Adv Mater 2019;31:1902352.
[3] Guo B. 2D noncarbon materials-based nonlinear optical devices for ultrafast photonics. Chin Opt Lett 2018;16:020004.
[4] Jiang XT, Zhang LJ, Liu SX, et al. Ultrathin metal–organic framework: an emerging broadband nonlinear optical material for ultrafast photonics. Adv Opt Mater 2018;6:1800561.
[5] Xu YJ, Shi Z, Shi XY, et al. Recent progress in black phosphorus and black-phosphorus-analogue materials: properties, synthesis and applications. Nanoscale 2019;11:14491–527.
[6] Wang ZT, Chen Y, Zhao CJ, et al. Switchable dual-wavelength synchronously Q-switched erbium-doped fiber laser based on graphene saturable absorber. IEEE Photonics J 2012;4:869–76.
[7] Xu NN, Ming N, Han XL, et al. Large-energy passively Q-switched Er-doped fiber laser based on CVD-Bi_2Se_3 as saturable absorber. Opt Mater Express 2019;9:373–83.
[8] Wang T, Guo YL, Wan PB, et al. Flexible transparent electronic gas sensors. Small 2016;12:3748–56.
[9] Lu J, Zhang K, Liu XF, et al. Order-disorder transition in a two-dimensional boron-carbon-nitride alloy. Nat commun 2013; 4:1–7.
[10] Xie HH, Li ZB, Sun ZB, et al. Metabolizable ultrathin Bi_2Se_3 nanosheets in imaging-guided photothermal therapy. Small 2016;12:4136–45.
[11] Yang S, Liu YL, Chen W, et al. High sensitivity and good selectivity of ultralong MoO_3 nanobelts for trimethylamine gas. Sensor Actuat B-Chem 2016;226:478–85.
[12] Lu L, Tang X, Cao R, et al. Broadband nonlinear optical response in few-layer antimonene and antimonene quantum dots: a promising optical Kerr media with enhanced stability. Adv Optical Mater 2017;5:1700301.
[13] Huang ZY, Zhang Z, Qi X, et al. Wall-like hierarchical metal oxide nanosheet arrays grown on carbon cloth for excellent supercapacitor electrodes. Nanoscale 2016;8:13273–9.
[14] Zhang YP, Lim CK, Dai ZG, et al. Photonics and optoelectronics using nano-structured hybrid perovskite media and their optical cavities. Phys Rep 2019;795:1–51.
[15] Zhao LM, Tang DY, Wu X, et al. Dissipative soliton generation in Yb-fiber laser with an invisible intracavity bandpass filter. Opt Lett 2010;35:2756–8.
[16] Zhang HN, Liu J. Gold nanobipyramids as saturable absorbers for passively Q-switched laser generation in the 1.1 μm region. Opt Lett 2016;41:1150–2.
[17] Liu J, Chen Y, Tang PH, et al. Generation and evolution of mode-locked noise-like square-wave pulses in a large-anomalous-dispersion Er-doped ring fiber laser. Opt Express 2015;23:6418–27.
[18] Zhao LM, Tang DY, Zhang H, et al. Soliton trapping in fiber lasers. Opt Express 2008;16:9528–33.
[19] Zhang H, Tang DY, Zhao LM, et al. Induced solitons formed by cross-polarization coupling in a birefringent cavity fiber laser. Opt Lett 2008;33:2317–9.
[20] Ming N, Tao SN, Yang WQ, et al. Mode-locked Er-doped fiber laser based on PbS/CdS core/shell quantum dots as saturable absorber. Opt Express 2018;26:9017–26.
[21] Song YF, Shi XJ, Wu CF, et al. Recent progress of study on optical solitons in fiber lasers. Appl Phys Rev 2019;6:021313.
[22] Bao QL, Zhang H, Wang Y, et al. Atomic-layer graphene as a saturable absorber for ultrafast pulsed lasers. Adv Funct Mater 2009;19:3077–83.
[23] Sun ZP, Hasan T, Torrisi F, et al. Graphene mode-locked ultrafast laser. ACS Nano 2010;4:803–10.
[24] Zhang H, Bao QL, Tang DY, et al. Large energy soliton erbium-doped fiber laser with a graphene-polymer composite mode locker. Appl Phys Lett 2009;95:141103.
[25] Popa D, Sun ZJ, Torrisi F, et al. Sub 200 fs pulse generation from a graphene mode-locked fiber laser. Appl Phys Lett 2010;97:203106.
[26] Zhang H, Tang DY, Knize RJ, et al. Graphene mode locked, wavelength-tunable, dissipative soliton fiber laser. Appl Phys Lett 2010;96:111112.
[27] Bao QL, Zhang H, Ni ZH, et al. Monolayer graphene as a saturable absorber in a mode-locked laser. Nano Res 2011;4:297–307.
[28] Zhang H, Tang DY, Zhao LM, et al. Large energy mode locking of an erbium-doped fiber laser with atomic layer graphene. Opt Express 2009;17:17630–5.
[29] Zhang H, Tang DY, Zhao LM, et al. Compact graphene mode-locked wavelength-tunable erbium-doped fiber lasers: from all anomalous dispersion to all normal dispersion. Laser Phys Lett 2010;7:591.
[30] Niu KD, Sun RY, Chen QY, et al. Passively mode-locked Er-doped fiber laser based on SnS_2 nanosheets as a saturable absorber. Photonics Res 2018;6:72–6.
[31] Zhang H, Lu SB, Zheng J, et al. Molybdenum disulfide (MoS_2) as a broadband saturable absorber for ultra-fast photonics. Opt Express 2014;22:7249–60.
[32] Liu H, Luo AP, Wang FZ, et al. Femtosecond pulse erbium-doped fiber laser by a few-layer MoS_2 saturable absorber. Opt Lett 2014;39:4591–4.
[33] Wu K, Zhang XY, Wang J, et al. WS_2 as a saturable absorber for ultrafast photonic applications of mode-locked and Q-switched lasers. Opt Express 2015;23:11453–61.
[34] Liu WJ, Pang LH, Han HN, et al. Tungsten disulphide for ultrashort pulse generation in all-fiber lasers. Nanoscale 2017;9:5806–11.
[35] Liu WJ, Liu ML, Yin JD, et al. Tungsten diselenide for all-fiber lasers with chemical vapor deposition method. Nanoscale 2018;10:7971–7.
[36] Liu WJ, Liu ML, Ou Yang YY, et al. Tungsten diselenide for mode-locked erbium-doped fiber lasers with short pulse duration. Nanotechnology 2018;29:174002.
[37] Ma PF, Lin W, Zhang HN, et al. High-power large-energy rectangular mode-locked Er-doped fiber laser based on high-damage-threshold MoS_2saturable absorber. IEEE Photonics J 2019;11:1–12.
[38] Liu JS, Li XH, Guo YX, et al. Harmonic mode-locking: $SnSe_2$nanosheets for subpicosecond harmonic mode-locked pulse generation. Small 2019;15:1902811.
[39] Niu KD, Chen QY, Sun RY, et al. Passively Q-switched erbium-doped fiber laser based on SnS_2 saturable absorber. Opt Mater Express 2017;7:3934–43.
[40] Xie ZJ, Zhang F, Liang ZM, et al. Revealing of the ultrafast third-order nonlinear optical response and enabled photonic application in two-dimensional tin sulfide. Photonics Res 2019;7:494–502.

[41] Hu QY, Zhang XY, Liu ZJ, et al. High-order harmonic mode-locked Yb-doped fiber laser based on a $SnSe_2$ saturable absorber. Opt Laser Technol 2019;119:105639.
[42] Liu H, Zheng XW, Liu M, et al. Femtosecond pulse generation from a topological insulator mode-locked fiber laser. Opt Express 2014;22:6868–73.
[43] Sotor J, Sobon G, Abramski KM. Sub-130 fs mode-locked Er-doped fiber laser based on topological insulator. Opt Express 2014;22:13244–9.
[44] Chen Y, Wu M, Tang PH, et al. The formation of various multi-soliton patterns and noise-like pulse in a fiber laser passively mode-locked by a topological insulator based saturable absorber. Laser Phys Lett 2014;11:055101.
[45] Yan PG, Lin RY, Chen H, et al. Topological insulator solution filled in photonic crystal fiber for passive mode-locked fiber laser. IEEE Photonics Technol Lett 2014;27:264–7.
[46] Mu HR, Wang ZT, Yuan J, et al. Graphene-Bi_2Te_3 heterostructure as saturable absorber for short pulse generation. Acs Photonics 2015;2:832–41.
[47] Sotor J, Sobon G, Grodecki K, et al. Mode-locked erbium-doped fiber laser based on evanescent field interaction with Sb_2Te_3 topological insulator. Appl Phys Lett 2014;104:251112.
[48] Ma PF, Lin W, Zhang HN, et al. Nonlinear absorption properties of $Cr_2Ge_2Te_6$ and its application as an ultra-fast optical modulator. Nanomaterials 2019;9:789.
[49] Guo LG, Shang XX, Zhao R, et al. Nonlinear optical properties of ferromagnetic insulator $Cr_2Ge_2Te_6$ and its application for demonstrating pulsed fiber laser. Appl Phys Express 2019;12:082006.
[50] Fu SG, Shang XX, Zhang F, et al. Ferromagnetic insulator $Cr_2Ge_2Te_6$ as a modulator for generating near-infrared bright-dark soliton pairs. Appl Opt 2019;58:9217–23.
[51] Feng JJ, Li XH, Shi ZJ, et al. 2D ductile transition metal chalcogenides (TMCs): novel high-performance Ag_2S nanosheets for ultrafast photonics. Adv Opt Mater 2019;1901762.
[52] Shi ZJ, Xu WX, Li XH, et al. Cuprous sulfide for different laser pulse generation: Q-switching and mode-locking. J Phys Chem C 2019;123:28370–6.
[53] Jhon YI, Koo J, Anasori BA, et al. Metallic MXene saturable absorber for femtosecond mode-locked lasers. Adv Mater 2017;29:1702496.
[54] Jiang XT, Liu SX, Liang WY, et al. Broadband nonlinear photonics in few-layer MXene $Ti_3C_2T_x$ (T=F, O, or OH). Laser Photonics Rev 2018;12:1700229.
[55] Wu Q, Jin X, Chen S, et al. MXene-based saturable absorber for femtosecond mode-locked fiber lasers. Opt Express 2019;27:10159–70.
[56] Wang L, Li XH, Wang C, et al. Few-layer Mxene $Ti_3C_2T_x$ (T=F, O, Or OH) for robust pulse generation in a compact Er-doped fiber laser. ChemNanoMat 2019;5:1233–8.
[57] Zhang M, Wu Q, Zhang F, et al. 2D black phosphorus saturable absorbers for ultrafast photonics. Adv Optical Mater 2019;7:1800224.
[58] Wu L M, Xie ZJ, Lu L, et al. Few-layer tin Sulfide: a promising black-phosphorus-analogue 2D material with exceptionally large nonlinear optical response, high stability, and applications in all-optical switching and wavelength conversion. Adv Opt Mater 2018;6:1700985.
[59] Chen Y, Jiang GB, Chen SQ, et al. Mechanically exfoliated black phosphorus as a new saturable absorber for both Q-switching and mode-locking laser operation. Opt Express 2015;23:12823–33.
[60] Luo ZC, Liu M, Guo ZN, et al. Microfiber-based few-layer black phosphorus saturable absorber for ultra-fast fiber laser. Opt Express 2015;23:20030–9.
[61] Chen Y, Chen SQ, Liu J, et al. Sub-300 femtosecond soliton tunable fiber laser with all anomalous dispersion passively mode locked by black phosphorus. Opt Express 2016;24:13316–24.
[62] Sotor J, Sobon G, Macherzynski W, et al. Black phosphorus saturable absorber for ultrashort pulse generation. Appl Phys Lett 2015;107:051108.
[63] Xu YH, Jiang XF, Ge YQ, et al. Size-dependent nonlinear optical properties of black phosphorus nanosheets and their applications in ultrafast photonics. J Mater Chem C 2017;5:3007–13.
[64] Mao D, Li MK, Cui XQ, et al. Stable high-power saturable absorber based on polymer-black-phosphorus films. Opt Commun 2018;406:254–9.
[65] Song YF, Chen S, Zhang Q, et al. Vector soliton fiber laser passively mode locked by few layer black phosphorus-based optical saturable absorber. Opt Express 2016;24:25933–42.
[66] Jin XX, Hu GH, Zhang M, et al. 102 fs pulse generation from a long-term stable, inkjet-printed black phosphorus-mode-locked fiber laser. Opt Express 2018;26:12506–13.
[67] Zhao Y, Guo PL, Li XH, et al. Ultrafast photonics application of graphdiyne in optical communication region. Carbon 2019;149:336–41.
[68] Song YF, Liang ZM, Jiang XT, et al. Few-layer antimonene decorated microfiber: ultra-short pulse generation and all-optical thresholding with enhanced long term stability. 2D Mater 2017;4:045010.
[69] Lu L, Liang ZM, Wu LM, et al. Few-layer bismuthene: sonochemical exfoliation, nonlinear optics and applications for ultrafast photonics with enhanced stability. Laser Photonics Rev 2018;12:1700221.
[70] Guo B, Wang SH, Wu ZX, et al. Sub-200 fs soliton mode-locked fiber laser based on bismuthene saturable absorber. Opt Express 2018;26:22750–60.
[71] Wang C, Wang L, Li XH, et al. Few-layer bismuthene for femtosecond soliton molecules generation in Er-doped fiber laser. Nanotechnology 2018;30:025204.
[72] Xu NN, Ma PF, Fu SG, et al. Tellurene-based saturable absorber to demonstrate large-energy dissipative soliton and noise-like pulse generations. Nanophotonics 2020; DOI: https://doi.org/10.1515/nanoph-2019-0545.
[73] Guo J, Zhao JL, Huang DZ, et al. Two-dimensional tellurium-polymer membrane for ultrafast photonics. Nanoscale 2019;11:6235–42.
[74] Xing CY, Xie ZJ, Liang ZM, et al. 2D nonlayered selenium nanosheets: facile synthesis, photoluminescence, and ultrafast photonics. Adv Opt Mater 2017;5:1700884.
[75] Sun JF, Shi HL, Siegrist T, et al. Electronic, transport, and optical properties of bulk and mono-layer $PdSe_2$. Appl Phys Lett 2015;107:153902.
[76] Long MS, Wang Y, Wang P, et al. Palladium diselenide long-wavelength infrared photodetector with high sensitivity and stability. ACS Nano 2019;13:2511–9.
[77] Qin D, Yan P, Ding GQ, et al. Monolayer $PdSe_2$: a promising two-dimensional thermoelectric material. Sci Rep 2018;8:1–8.
[78] Liang QJ, Wang QX, Zhang Q, et al. High-performance, room temperature, ultra-broadband photodetectors based on air-stable $PdSe_2$. Adv Mater 2019;31:1807609.

[79] Sun ML, Chou JP, Shi LH, et al. Few-layer $PdSe_2$ sheets: promising thermoelectric materials driven by high valley convergence. ACS Omega 2018;3:5971–9.
[80] Oyedele A, Yang SZ, Liang LB, et al. $PdSe_2$: pentagonal two-dimensional layers with high air stability for electronics. J Am Chem Soc 2017;139:14090–97.
[81] Zeng LH, Wu D, Lin SH, et al. Controlled synthesis of 2D palladium diselenide for sensitive photodetector applications. Adv Funct Mate 2019;29:1806878.
[82] Xie ZJ, Xing CY, Huang WC, et al. Ultrathin 2D nonlayered tellurium nanosheets: facile liquid-phase exfoliation, characterization, and photoresponse with high performance and enhanced stability. Adv Funct Mater 2018;28:1705833.
[83] Huang WT, Xie ZJ, Fan TJ, et al. Black-phosphorus-analogue tin monosulfide: an emerging optoelectronic two-dimensional material for high-performance photodetection with improved stability under ambient/harsh conditions. J Mater Chem C 2018;6:9582–93.
[84] Li ZQ, Dong NN, Wang J, et al. Generation of multi-gigahertz laser pulses in optical lattice-like cladding waveguides with $PdSe_2$ as a new saturable absorber. 2019 Conference on Lasers and Electro-Optics Europe & European Quantum Electronics Conference (CLEO/Europe-EQEC) IEEE 2019;1:1.
[85] Ma YF, Zhang SC, Ding SJ, et al. Passively Q-switched Nd:$GdLaNbO_4$ laser based on 2D $PdSe_2$ nanosheet. Opt Laser Technol 2020;124:105959.
[86] Perdew JP, Zunger A. Self-interaction correction to density functional approximation for many electron systems. Phys Rev B 1981;23:5048.
[87] Kresse G, Joubert D. From ultrasoft pseudopotentials to the projector augmented-wave method. Phys Rev B 1999;59:1758.
[88] Perdew JP, Burke K, Ernzerhof M. Generalized gradient approximation made simple. Phys Rev Lett 1996;77:3865.
[89] Klimeš J, Bowler DR, Michaelides A. Chemical accuracy for the van der Waals density functional. J Phys: Condens Matter 2009;22:022201.
[90] Grimme S. Semiempirical GGA-type density functional constructed with a long-range dispersion correction. J Comput Chem 2006;27:1787–99.
[91] Grimme S, Antony J, Ehrlich S, et al. A consistent and accurate ab initio parametrization of density functional dispersion correction (DFT-D) for the 94 elements H-Pu. J Chem Phys 2010;132:154104.
[92] Tkatchenko A, Scheffler M. Accurate molecular van der Waals interactions from ground-state electron density and free-atom reference data. Phys Rev Lett 2009;102:073005.
[93] Song YF, Li L, Tang DY. Quasi-periodicity of vector solitons in a graphene mode-locked fiber laser. Laser Phys Lett 2013;10:125103.
[94] Song YF, Liang ZM, Zhang H, et al. Period-doubling and quadrupling bifurcation of vector soliton bunches in a graphene mode locked fiber laser. IEEE Photonics J 2017;9:1–8.